ADVANCED FUNCTIONAL MATERIALS
www.afm-journal.de

Nanoassembly Growth Model for Subdomain and Grain Boundary Formation in 1T′ Layered ReS_2

Xiaobo Li, Xiao Wang, Jinhua Hong, Dongyan Liu, Qingliang Feng, Zhibin Lei, Kaihui Liu, Feng Ding,* and Hua Xu**

Grain boundaries (GBs) significantly affect the electrical, optical, magnetic, and mechanical properties of 2D materials. An anisotropic 2D material like ReS_2 provides unprecedented opportunities to explore novel GB properties, since the reduced lattice symmetry offers greater degrees of freedom to build new GB structures. Here the atomic structure and formation mechanism of unusual multidomain and diverse GB structures in the vapor phase synthesized ReS_2 atomic layers are reported. Using high-resolution electron microscopy, two major categories of GBs are observed in each ReS_2 domain, namely, the joint GB including three structures, and the GBs formed from a reconstruction of Re4-chains including seven different structures. Based on the experimental observations, a novel "nanoassembly growth model" is proposed to elucidate the growth process of ReS_2, where three types of Re4-chain reconstruction give rise to a multidomain structure. Moreover, it is shown that by controlling the thermodynamics of the growth process, the structure and density of GB in the ReS_2 domain can be tailored. First-principles calculations point to interesting new properties resulting from such GBs, such as a new electron state or ferromagnetism, which are highly sought after in the construction of novel 2D devices.

1. Introduction

Grain boundaries (GBs) greatly modify material properties including its electrical, optical, magnetic, and mechanical responses and have therefore been a hot topic of research in the field of materials science.[1,2] In a 2D material where the thickness is reduced to one or several atom layers, GBs are expected to have a prominent effect on properties and thereby directly impact applications of these materials.[3,4] In general, GBs act as scattering sites for carriers and degrade transport by forming electrostatic barriers,[4] and are therefore deleterious to achieve high-performance in 2D electronics.[5] On the other hand, GBs can also provide a platform to explore emerging properties that are not manifest in a single crystal, since atomic displacement at a GB can modify its electronic state to a large extent.[6–10] In this regard, an in-depth understanding of the formation mechanism of GBs in 2D materials at the atomic scale is crucial to tailor material properties in a controllable way, for example, to eliminate unwanted GBs or to create and exploit specific types of GBs. Recently, significant progress has been made on the formation, atomic structure and properties of GBs in 2D materials, but so far, these works have mainly focused on high-symmetry 2D materials like graphene, hexagonal boron nitride and transition metal dichalcogenides (TMDs).[11–16]

As one type of counterpart, low-symmetry 2D materials (such as ReS_2, $ReSe_2$, GaTe, and 1T′ $MoTe_2$) which are distinctly different from high-symmetry 2D materials,[17–22] would provide

X. B. Li, D. Y. Liu, Prof. Z. B. Lei, Prof. H. Xu
Key Laboratory of Applied Surface and Colloid Chemistry
Ministry of Education
Shaanxi Key Laboratory for Advanced Energy Devices
Shaanxi Engineering Lab for Advanced Energy Technology
School of Materials Science and Engineering
Shaanxi Normal University
Xi'an 710119, P. R. China
E-mail: xuhua-nano@snnu.edu.cn

Dr. X. Wang, Prof. F. Ding
Center for Multidimensional Carbon Materials
Institute for Basic Science
School of Materials Science and Engineering
Ulsan National Institute of Science and Technology
Ulsan 44919, South Korea
E-mail: f.ding@unist.ac.kr, gniding@gmail.com

Dr. J. H. Hong
Nanostructures Research Laboratory
Japan Fine Ceramics Center
Atsuta, Nagoya 456-8587, Japan
E-mail: jinhuahong436@gmail.com

Dr. Q. L. Feng
School of Science
Northwestern Polytechnical University
Xi'an 710072, P. R. China

Prof. K. H. Liu
State Key Laboratory for Mesoscopic Physics
Collaborative Innovation Center of Quantum Matter
School of Physics
Peking University
Beijing 100871, China

The ORCID identification number(s) for the author(s) of this article can be found under https://doi.org/10.1002/adfm.201906385.

DOI: 10.1002/adfm.201906385

colossal opportunities to explore novel GB structures and properties. ReS_2, for example, forms a distorted octahedral (1T′) structure with triclinic symmetry as a result of charge decoupling from the extravalence electron of the Re atom.[23] The low-symmetry structure endows ReS_2 strong in-plane anisotropic electrical, optical, and vibrational properties,[24,25] which enables its application in field-effect transistors, polarized light photodetectors, integrated inverter circuits, and polarization controllers.[26–29] Furthermore, the reduction of lattice symmetry of ReS_2 could offer more degrees of freedom for building new GB structures and exploring their properties.

Here, we present experimental results from polarized optical and Raman imaging, scanning transmission electron microscopy (STEM) and simulated results from density functional theory (DFT) to demonstrate the formation of subdomains, GBs and even superlattices in 1T′ ReS_2 layered material. Using polarized optical imaging, we can readily distinguish all the subdomains and GBs and assess their density in CVD-grown ReS_2. Combined with STEM and DFT calculation, we elucidated the atomic structure of the multidomain ReS_2 and revealed the Re4-chain reconstruction-derived "nanoassembly growth" mechanism. Based on this growth model, we were able to modulate the type and density of GBs in ReS_2 by tuning the growth thermodynamics, and even constructed coherent twin boundary superlattices, a novel structure in 2D materials. Moreover, electrical measurements show that the effect of coherent twin boundary on the electrical conductivity of ReS_2 is relatively weak when compared to that of joint GBs. DFT calculation point to new electronic state or ferromagnetic properties arising in these diverse GBs, which provides opportunities for GB-mediated engineering of material properties and applications.

2. Results and Discussion

It is necessary to have a clear understanding of the structural features of ReS_2 before investigating its GB structure and growth behavior. **Figure 1**a shows the valence electron structure of the Re atom in 1T′ ReS_2. In contrast to Mo ($4d^5 5s^1$) and W ($5d^4 6s^2$) elements in the more widely studied MoS_2 and WS_2, the extranuclear electron configuration of Re ($5d^5 6s^2$) reveals the presence of an extravalence electron. In ReS_2, the $5d^3$ orbital of Re^{4+} with octahedral coordination are split into e_g ($d_{x^2-y^2}$, d_{z^2}) and t_{2g} (d_{xy}, d_{xz}, d_{yz}), where the configuration with three valence electrons filled in the three degenerate states of

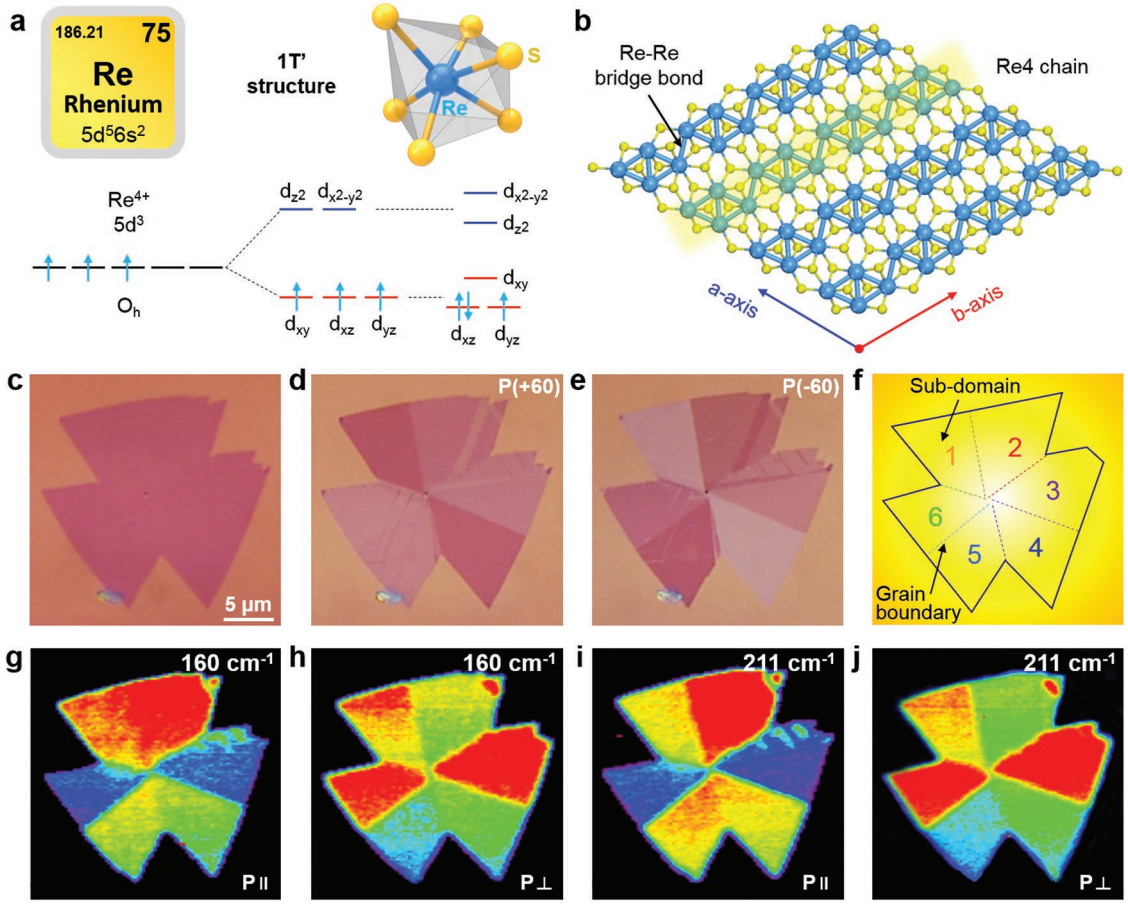

Figure 1. Subdomains and GBs in CVD-grown monolayer ReS_2. a) Valence electron structure of Re in 1T′ ReS_2. b) Schematic atomic structure of 1T′ ReS_2. c) OM image of a single CVD-grown monolayer ReS_2 domain, and the corresponding ARPOM images taken at the angle of d) 60° and e) –60° between polarizer and analyzer. g–j) Polarized Raman mapping images of the ReS_2 domain for the vibrational modes at 160 and 211 cm^{-1} under parallel (*xx*) and perpendicular (*xy*) polarization configuration, respectively.

t_{2g} is energetically unfavorable. Due to the Jahn–Teller effect, the t_{2g} energy levels are further split to eliminate the electronic degenerate state, leading ReS_2 to adopt a distorted 1T′ structure with low lattice symmetry.[30,31] As a result, all of its valence electrons are involved in metal–metal bonds, leading to formation of diamond-shaped Re4 clusters which are further linked by Re–Re bridge-bonds to form anisotropic Re4-chains, defined as *b*-axis (Figure 1b). It is this anisotropic structure that causes the unusual growth behavior of ReS_2, and thereby generates a variety of intricate morphologies and microstructures, as will be discussed below.

Monolayer ReS_2 film was synthesized via CVD growth, see details in the Experimental Section. Figure 1c shows the optical microscopy (OM) image of a typical CVD-grown monolayer ReS_2 domain, it appears as if the ReS_2 domain is similar to most CVD-grown 2H TMDs, where each domain is a single crystal. However, the ReS_2 domain is in fact, composed of several subdomains, which can be visualized by angle-resolved polarized optical microscopy (ARPOM) imaging, an imaging technique we developed for the first time for imaging the microstructures in low-symmetry 2D materials. The setup for the ARPOM imaging is shown in Figure S1 of the Supporting Information, where a polarizer and an analyzer with tunable angle are placed at the incident and collection light paths, respectively. This technique takes advantage of the anisotropic nature of ReS_2, which gives rise to notable differences in the refractive index and light absorption in different crystalline axes directions. As a result, six subdomains and the corresponding GBs can be readily distinguished in the ReS_2 domain from their optical contrast measured under different polarization as shown in Figure 1d,e. Using ARPOM imaging, we can thus quickly distinguish all the subdomains and GBs in ReS_2 domains with arbitrarily complex morphologies (Figure S1, Supporting Information).

The above results demonstrate that a CVD-grown ReS_2 domain is composed of several subdomains with different lattice orientations, and GBs are formed between these subdomains, as schematically shown in Figure 1f. Similar results are also observed from polarized Raman mapping of the two primary vibration modes at 160 and 211 cm^{-1} measured under parallel-polarized ($P_{//}$) and cross-polarized ($P_{\perp}$) light (Figure 1g–j). Notably, unlike GBs generated in polycrystalline graphene and 2H TMDs (such as MoS_2 and WS_2) by splicing different domains grown from several nucleation sites,[3,15,16] the GBs in ReS_2 domain are grown from one nucleation center. Several previous works have noticed this unusual structural feature in CVD-grown ReS_2 and $ReSe_2$ using polarized Raman spectroscopy and scanning probe microscopy.[32–34] More importantly, such multidomain structures are also observed in CVD-grown GaTe, and 1T′ $MoTe_2$/WTe_2,[18,35] indicating a common structural feature and similar growth behavior of these low-symmetry 2D materials. However, the atomic microstructure of ReS_2 domain is still unclear, especially with respect to how the subdomains and GBs are formed in space and in energy scale remains unexplored, which is critical to tailor material properties in a controllable way.

We studied the atomic structure of ReS_2 subdomains using aberration-corrected annular dark field scanning transmission electron microscopy (ADF-STEM) and angle-resolved polarized Raman spectroscopy (ARPRS). **Figure 2**a shows the ADF-STEM image of a single ReS_2 domain with a triangular shape, where the two edges are marked by white dotted lines. Two subdomains with a line GB are clearly observed in the corresponding POM image of the ReS_2 domain (inset in Figure 2a), defined as domain A and domain B. High-resolution ADF-STEM images of the two subdomains show the typical 1T′ structure of ReS_2 with a visible Re4-chain (Figure 2b). Note that the in-plane orientation (*b*-axis direction) of two adjacent subdomains (marked by two pink lines) forms an angle of 60°. Moreover, the macroscopic line GB observed in ARPOM image (inset of Figure 2a) displays a broken line (white line in Figure 2b) feature at the atomic scale. Notably, three types of interface structures with different atomic arrangements, defined as type i, ii, and iii GB, are observed at the GB (Figure S2, Supporting Information). The diverse GB structures together with the broken line feature suggest that the GB in ReS_2 domain is formed by jointing the two subdomains with in-plane orientation at 60° angle.

In addition to the in-plane orientation, due to its low-symmetry, ReS_2 has only one inversion center and consequently, should have two reverse vertical orientations: "up" and "down."[36] In this regard, identifying the vertical orientation of each subdomain is critical to completely understand the structural features of CVD-grown ReS_2. Here, we studied the vertical orientations of the two subdomains from ARPRS which has been proven to be an effective way to identify it.[36] Raman spectra as a function of the laser polarization angle acquired at domain A and domain B are shown in Figure 2c,d. The opposite trend in Raman intensity of A_{1g} (150 cm^{-1}), B_{2g} (160 cm^{-1}), and A_{2g} (211 cm^{-1}) modes as function of the laser polarization angle for the two subdomains indicates that they have a 180° inversion symmetry in the vertical orientation with respect to each other, as schematically shown in Figure 2e,f. Actually, the vertical orientations of the two adjacent subdomains in ReS_2 domain are not always opposite (sometimes they are the same (0°)), conforming to its growth mechanism which will be discussed below. The above results while answered the query about the vertical orientation of CVD-grown ReS_2 proposed in previously reported work,[36] also throws light on the relationship between in-plane and vertical orientation of the adjacent two subdomains.

Overall, each pair of adjacent subdomains in CVD-grown ReS_2 forms a 60° angle in the in-plane orientation, with 0° or 180° inversion symmetry in the vertical orientation, giving rise to the jointed GBs with three types of interface structure. As emphasized earlier, the multidomain ReS_2 structure is actually grown from a single nucleation center. At this point, it is pertinent to ask: how does ReS_2 grow into such an unusual structure? In addition, in keeping with the 1T′ structure of ReS_2, the intrinsic morphology of CVD-grown ReS_2 should be a rhombus or a rectangle instead of a hexagon and triangle that is usually observed.[32,37] This however appears to be a common query in above mentioned CVD-grown low-symmetry 2D materials.

To get an insight into the formation of multidomain ReS_2, we further studied its atomic structure using aberration-corrected STEM. Results show that are construction of the Re4-chain, caused just by a minor displacement of Re atoms from the perfect 1T′ structure during growth, results in the formation of a series of new types of GBs in ReS_2 (**Figure 3**a–c). To fully understand the structure of ReS_2, we predicted all the possible GB

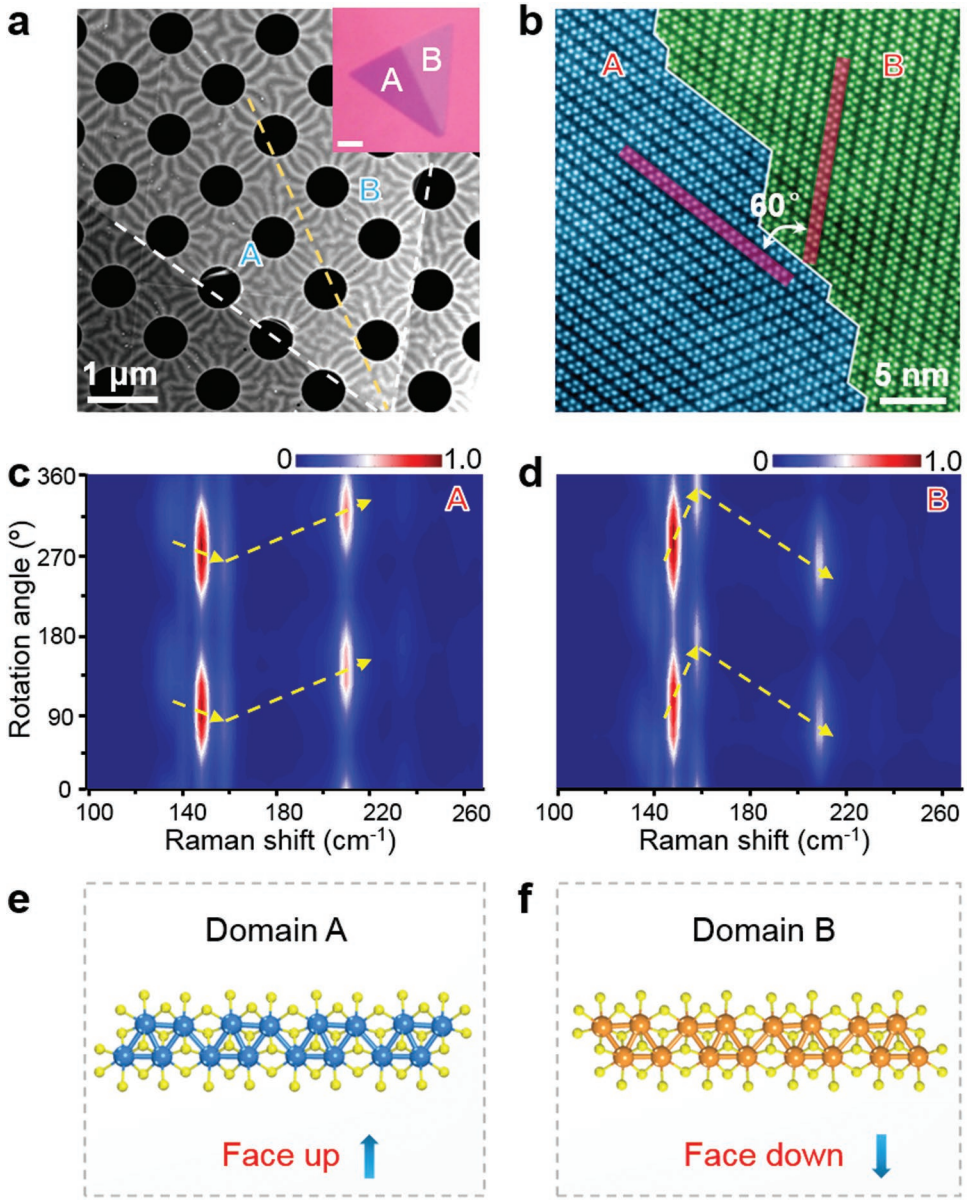

Figure 2. In-plane and vertical lattice orientations of subdomains in CVD-grown ReS_2. a) DF-TEM images of a monolayer ReS_2 domain; inset is the corresponding POM image. b) High-resolution ADF-STEM images taken at GB regions. 2D mapping of the Raman spectral intensity with respect to the rotation angle measured at c) domain A and d) domain B; the intensity is normalized with respect to the strongest peak at 150 cm^{-1}. Structure models of e) domain A and f) domain B showing the two different vertical orientations: face up and face down.

structures and calculated their formation energies (Figure 3d) using DFT, and defined them according to the lattice orientation of adjacent subdomains (Figures S3 and S4 and Table S1, Supporting Information). Experimentally, we discovered seven types of GBs in CVD-grown ReS_2, representing seven different Re4-chain reconstructions (Figure S5, Supporting Information). Among them, three types of GBs including $(0°, 0°)_\sigma$, $(60°, 120°)_\sigma$, and $(120°, 240°)_\sigma$ are the most commonly observed according to our statistical analysis (Figure 3e), while the other four types are only occasionally observed. In the case of the $(0°, 0°)_\sigma$ GB shown in Figure 3a, the two subdomains are separated by a coherent twin boundary, where one Re4 cluster is shared by two domains. The in-plane orientations of the two subdomains form an angle of 120°, while their vertical orientation shows 180° inversion symmetry. For the $(60°, 120°)_\sigma$ GB in Figure 3b, the two subdomains are separated by an incoherent twin boundary, where the in-plane orientations of the two domains are at 120° angle with a tiny dislocation, and their vertical orientation shows 180° inversion symmetry. For the $(120°, 240°)_\sigma$ GB in Figure 3c, the in-plane orientation of the two domains are at an angle of 0°, while the vertical orientation shows 180° inversion symmetry. Thus, the $(120°, 240°)_\sigma$ GB and the corresponding two subdomains are difficult to distinguish from ARPOM and polarized Raman imaging.

The atomistic mechanism for the reconstruction of Re4-chains during ReS_2 growth can be understood both from the

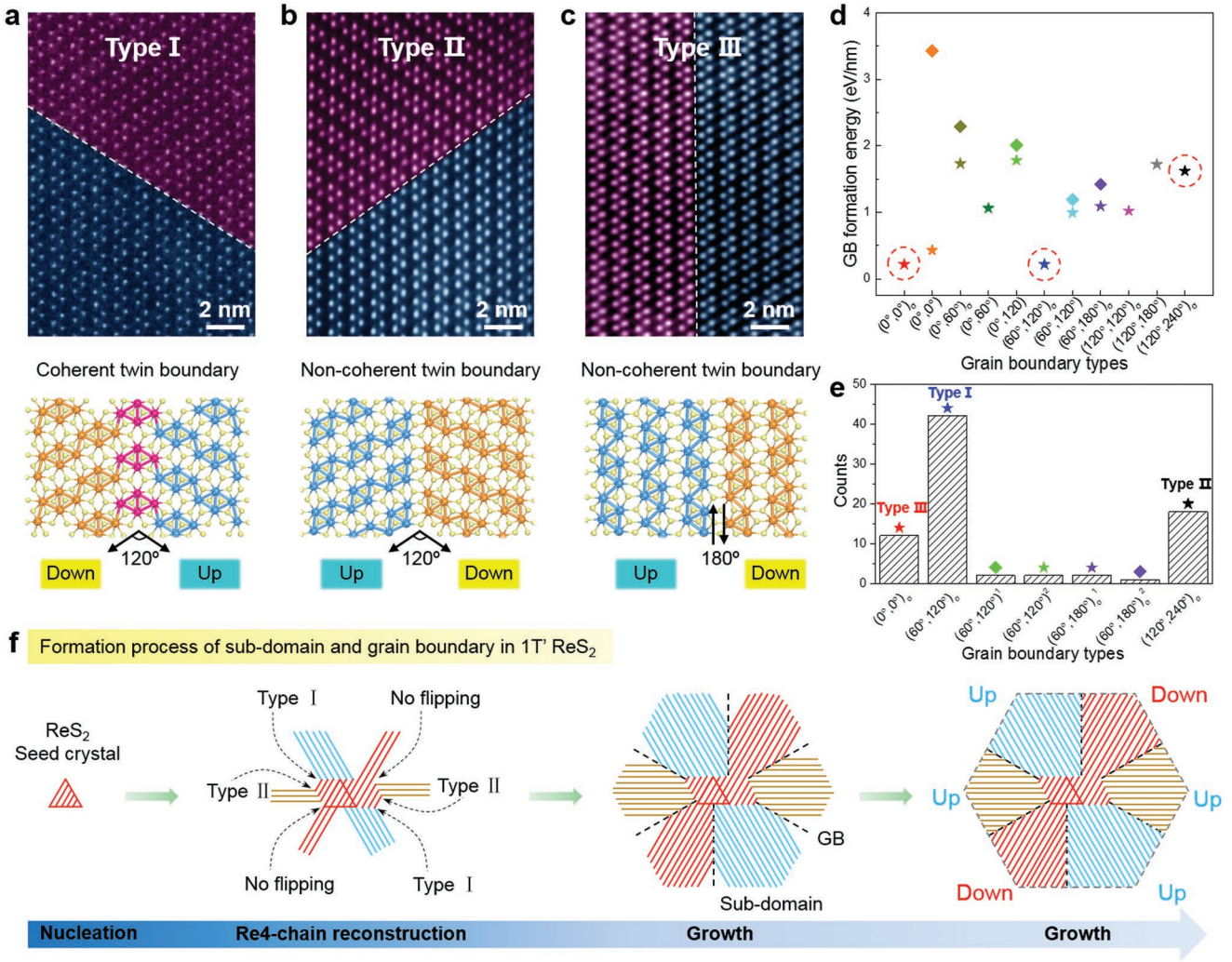

Figure 3. Formation of subdomains and GBs in CVD-grown ReS_2 by reconstruction of Re4-chains. High-resolution ADF-STEM images of a) type I, b) type II, and c) type III GBs seen in CVD-grown ReS_2, given below each STEM image is the corresponding structure model. d) DFT-calculated formation energy and e) statistical frequency of the different types of GB. f) Schematic diagram showing the formation process of subdomains and GBs during ReS_2 growth.

deviation of atom bonding from its equilibrium state, and the strain field effect. Generally, in the growth of 2D materials, the atoms dock at the edges of material go through a sequence of nonequilibrium states with high energy barrier (E_b) where the atom bonding deviate from the perfect lattice structure (called stacking fault), and final stabilized into the materials lattice at equilibrium or nonequilibrium states is determined by the system energy.[38] In the lattice of high symmetry 2D materials, such as MoS_2, the presence of a stacking fault generally introduces only defects or dislocations since all the Mo/S atoms in one unit cell have the same bonding feature.[39] By contrast, in ReS_2 with a low-symmetry, since the Re/S atoms in one unit cell have different (but fixed) chemical environments and bonding, the introduction of a stacking fault inevitably leads to Re4-chain reconstruction. In addition, the strain field in the ReS_2 lattice induced by its lattice mismatch to the substrate would lead to its growth to be thermodynamically unfavorable. In such a case, a reconstruction of the Re4-chain accompanied by a change in the lattice orientation of ReS_2 and formation of GBs could be beneficial to release the lattice strain. This strain field effect was verified by growing ReS_2 on substrates with different lattice parameters, and it was observed that the GB density increases on substrates with greater lattice mismatch (Figure S6 and Table S2, Supporting Information). Analogously, the strain field effect was also proposed in a previous study to explain the Re4-chain flip observed in mechanical exfoliated ReS_2, which is induced by electron beam irradiation at high temperature.[24]

It is well known that a GB in itself has an energy state and the final structure of a GB is usually determined by its formation energy (E_f).[14,38] We therefore conducted DFT calculations to estimate E_f of the different types of GBs in ReS_2 domains (Figure 3d). It was found that the E_f of GBs formed via the reconstruction of Re4-chain (marked by red dashed circles) is overall lower than that of the joint GBs. Combine with the statistical results in Figure 3e, we infer that Re4-chain

reconstruction appears to be driven by the formation of low-energy GBs, since the type I, type II, and type III GBs are most commonly observed in our STEM results, which are a known energy-lowering mechanism. Notably, though type II GB has a relative higher E_f, it remains widely present in ReS_2 domains. We attribute this to kinetic factors, since E_b also determines the formation of GB.

Based on the above fact, we propose that it should be the three types of Re4-chain reconstructions result in the CVD-grown ReS_2 composed of several subdomains with different in-plane and vertical lattice orientations. Here, we present a comprehensive mechanism which we call "nanoassembly growth," to explain the formation process from nucleation to growth of ReS_2 multidomain structures as shown in Figure 3f. For convenience, we define the three types of Re4-chain reconstructions as type I, type II, and type III flips. In the initial nucleation stage, a seed crystal of ReS_2 resembles that of MoS_2, which is a single crystal. As the growth moves to the Re4-chain reconstruction stage, the two sides of a Re4-chain in the ReS_2 seed crystal can have three possible growth patterns: no flip, type I flip, and type II flip. The first allows ReS_2 to maintain the initial growth orientation, while the latter two change both the in-plane and vertical orientations by 120° and 180°, respectively. Here, we have not considered the type III flip, as it does not bring about the change of in-plane orientation. During further growth, the type I and type II flips cause the merging of each pair of adjacent subdomains that have a particular in-plane (60° angle) and vertical (0° or 180°) orientational relationship, which is consistent with the structural features of the joint GB shown in Figure 2. Finally, a hexagonal ReS_2 domain composed of six subdomains with different in-plane and vertical orientations are obtained, where both the twin boundary (mainly located in the nucleation region) and the joint GB (between each adjacent subdomain) are present. In some cases, the vertical orientations of a fraction of the subdomains may be different from the model structure, which is reasonable, since type III flip can also change the vertical orientation of ReS_2 (Figure S7, Supporting Information).

The entire growth of ReS_2 can thus be regarded as an ingenious nanoassembly process, and the obtained ReS_2 film can be seen as a complex multidomain architecture. In many cases, the three types of Re4-chain flips occur randomly during the structure reconstruction stage and the subsequent growth process, leading to complex and diverse morphologies, as well as structures of ReS_2. Previous works have not been able to explain the origin of these complex and versatile morphologies and have therefore simply attributed their formation to etching, anisotropic growth or off-symmetry growth.[40–42] Here, using the nanoassembly growth model, we can reasonably describe the growth process of ReS_2 with all different morphologies, as shown in Figure S8 of the Supporting Information. This is the first time that a feasible growth mechanism has been proposed for explaining the growth of ReS_2 multidomain structure. We believe this growth mechanism could be extended to understand the growth behavior of other low-symmetry 2D materials.

On the basis of our understanding as presented above, we have tried to modulate GB formation in ReS_2 by tuning its growth thermodynamics. The morphology and structure evolution of ReS_2 domains grown at different temperatures from 600 to 800 °C have been characterized by using OM and POM imaging as shown in **Figure 4**. A ReS_2 domain grown at 600 °C shows a regular hexagonal shape composed of six subdomains (Figure 4a), which is similar to previously reported works and is usually considered to be the ideal sample.[32,37,43] Nevertheless, we find that the lattice orientation is quite disordered in each subdomain, which in turn, appear to be composed of a large number of even smaller subdomains and GBs. This is because of the low growth temperature, at which, the thermal energy is not high enough to overcome the energy barrier for non-equilibrium atom bonding to return to its equilibrium state. As a result, the Re4-chains frequently reconstruct in various ways during the entire growth process, as verified by HRSTEM results in Figure S9 of the Supporting Information. By contrast, a high growth temperature can provide enough energy to enable atomic bonding to return to its equilibrium state. As expected, the morphology of ReS_2 domain changes irregular as growth temperature increases (Figure 4b), while the GB density in each subdomain is effectively decreased, and even single crystal subdomains are obtained at 700 °C (Figure 4c; Figure S9, Supporting Information). It is noted here that higher temperature (>750 °C) would increase the strain field in the ReS_2 lattice due to the difference of thermal expansion between ReS_2 and substrate, which is greater at higher temperatures. In such cases, continuous Re4-chain reconstruction with type I flips to decrease the energy of the system is preferred (Figure 4d,e; Figure S9, Supporting Information), resulting incoherent twin boundary superlattices (Figure 4e), a novel structure in 2D materials. Such superlattice structures in combination with the anisotropic feature of ReS_2, could give rise to many interesting optical and electrical properties. Notably, when subjected to postannealing treatments, the as-grown ReS_2 sample neither produces new GBs, nor eliminates existing GBs, indicating that Re4-chain reconstruction occurs during the growth of ReS_2 but not after the growth. The effective modulation of the density and type of GBs during ReS_2 growth provides a new opportunity for the controlled synthesis of highly crystalline ReS_2 with the desired structure.

Next, we studied the effect of subdomains and GBs on the optical and electrical properties of ReS_2 (**Figure 5**). ARPRS results show that ReS_2 grown at 700 °C displays strong anisotropy (Figure 5b), while that grown at 600 °C exhibits negligible anisotropy (Figure 5c). This result indicates that the large number of subdomains with different lattice orientations can degenerate its anisotropic optical properties to a great extent. The effect of GBs on the electrical transport properties of ReS_2 grown at different temperatures is shown in Figure 5a–c and Figure S10 (Supporting Information). It is found that the electrical conduction of ReS_2 grown at 700 °C is around ten times higher than that grown at 600 °C. We calculated the carrier mobility from the linear region of the transfer curves using the expression

$$\mu_{FET} = \frac{L}{W} \cdot \frac{1}{C_g \cdot V_{ds}} \cdot \frac{dI_{ds}}{dV_g} \quad (1)$$

where L and W are the length and width of the channel, respectively, and C_g is the back-gate capacitance of 300 nm thick SiO_2. It was found that the carrier mobility of ReS_2 grown at 700 °C

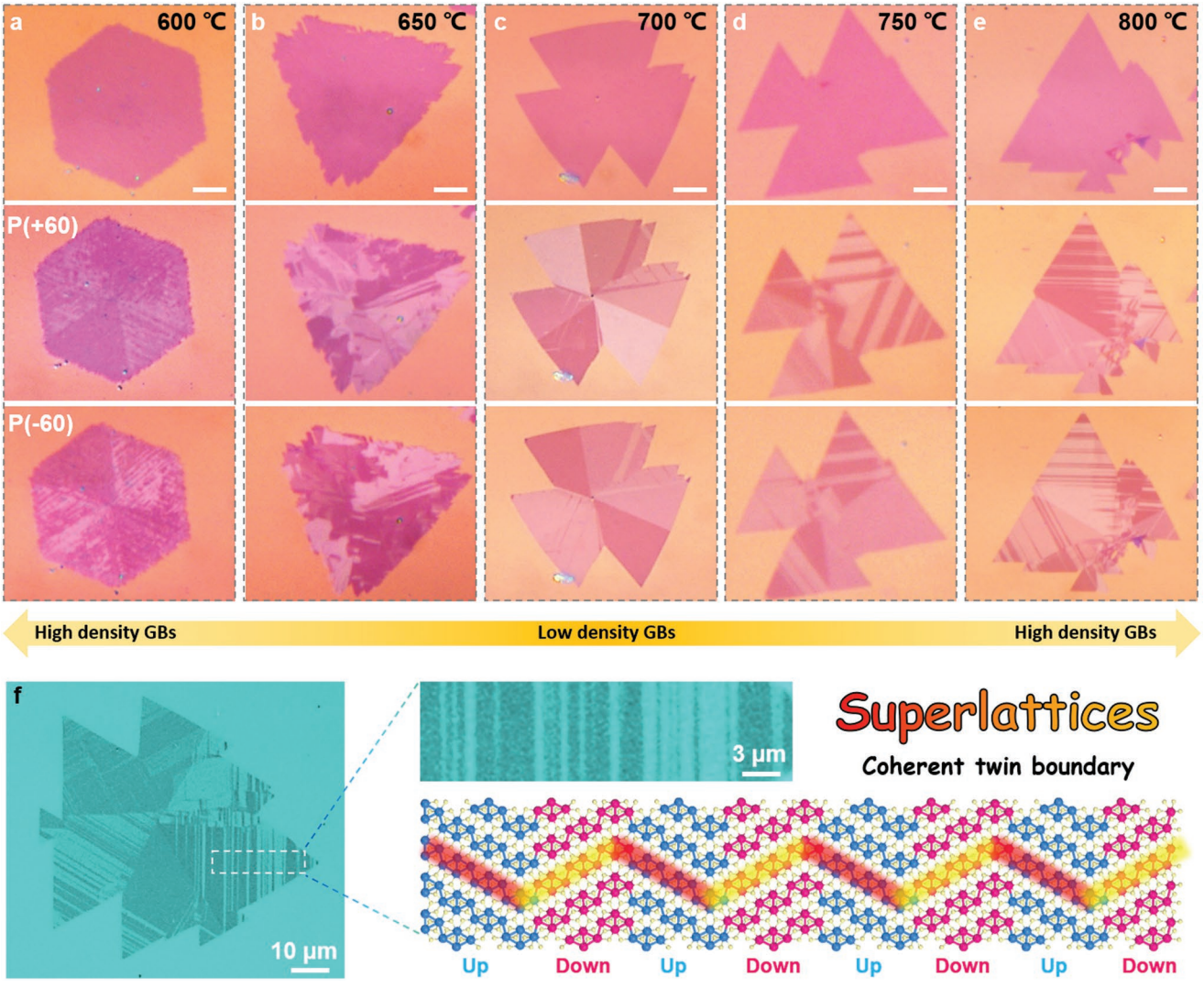

Figure 4. Thermodynamically modulated GB formation in CVD-growth of ReS_2. OM and POM images of monolayer ReS_2 grown at different temperatures: a) 600, b) 650, c) 700, d) 750, and e) 800 °C. f) Colored POM image of a ReS_2 domain grown at 800 °C and the corresponding structure model.

(≈3.4 $cm^2\ V^{-1}\ s^{-1}$) is nearly two orders of magnitude higher than that grown at 600 °C (≈0.1 $cm^2\ V^{-1}\ s^{-1}$). In addition, the current on on/off ratio of ReS_2 grown at 700 °C (≈10^6) is also larger than that grown at 600 °C (≈10^4). However, considering the extremely high GB density in ReS_2 domains grown at 600 °C, the two orders of magnitude decrease in mobility is not so large, since just one GB in graphene or MoS_2 has been found to decrease mobility by one order of magnitude, as reported in previous works.[4,44] Furthermore, the mobility of ReS_2 grown at 800 °C (≈0.8 $cm^2\ V^{-1}\ s^{-1}$) decreases just by a factor of 3–5 as compared to that grown at 700 °C, showing a very small dependence on the number of coherent twin boundaries. Hence, unlike the defect GB which strongly influences electrical properties in most of high-symmetry 2D materials, the GB in ReS_2 has a relatively smaller effect on carrier transport.

DFT simulation was performed to explore the properties of the different types of GBs as shown in Figure 5d–f. It is seen that the energy band structure of $(60°, 120°)_\sigma$ GBs is nearly same as that of single crystal ReS_2 (Figure 5d). This result is consistent with the very small effect of such GBs on electrical properties. Interestingly, several other GBs (such as $(0, 60)_\sigma$ GB and $(120, 240)_\sigma$ GB) give rise to novel properties, such as a new electronic state (Figure 5e) or ferromagnetism (Figure 5f), which are highly sought after in the conception of novel 2D electronic devices. An in-depth study on the electrical, photoelectrical, and magnetic properties of these various GBs is needed to be able to exploit them in practical devices.

In summary, this study reveals the novel and fascinating multidomain structure and formation mechanism of CVD-grown ReS_2 on the atomic scale. We demonstrate that ReS_2 domains are highly complex and composed of several subdomains with different in-plane and vertical orientations as well as a series of special GBs. The "nanoassembly growth" model proposed in this work is successful in describing the formation process of the complex ReS_2 domain structure. Our results significantly advance the understanding of the unusual structural features and growth behavior of 1T′ ReS_2 and can moreover,

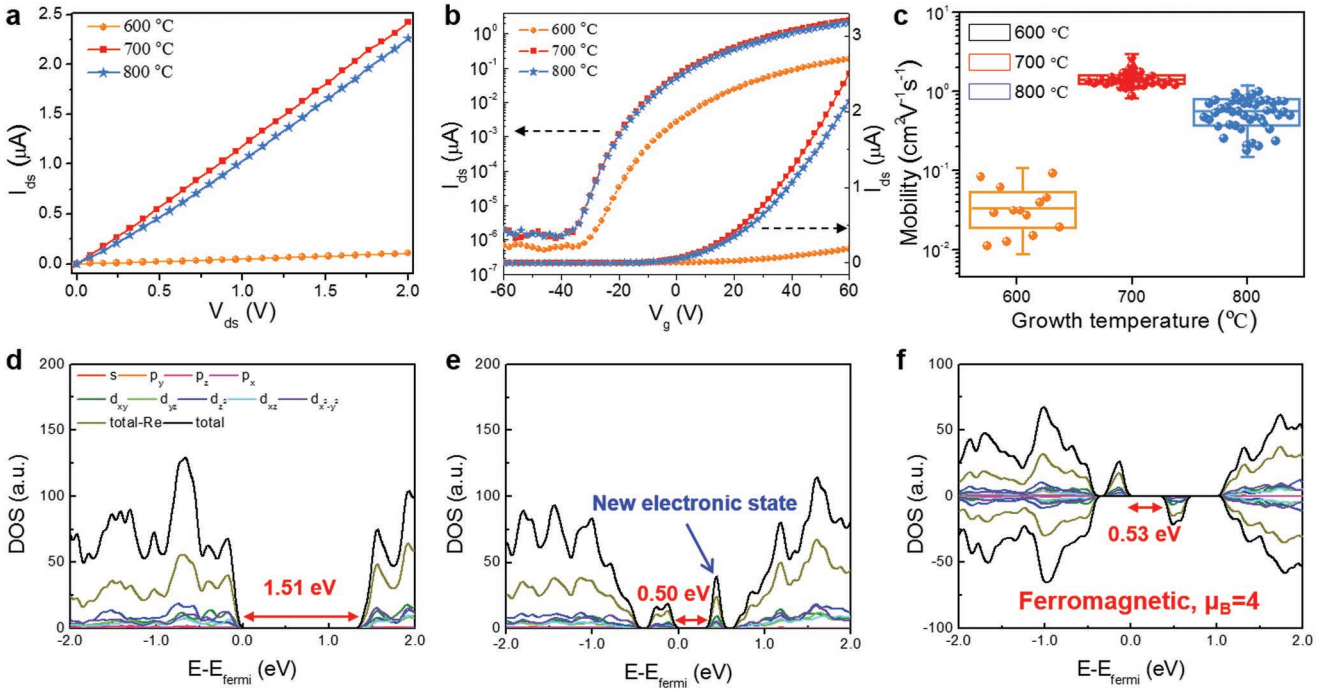

Figure 5. Effect of GBs on the electrical transport properties of ReS_2. a) Output curve and b) transfer curve of ReS_2 grown at 800, 700, and 600 °C. c) Statistical carrier mobilities of ReS_2 grown at 600, 700, and 800 °C. Devices of ReS_2 samples grown at different temperatures and corresponding output curves and transfer curves are shown in Figure S10 of the Supporting Information. d–f) Density of state (DOS) diverse GB structures: (d) $(60, 120)_{\sigma}$, (e) $(0, 60)_{\sigma}$, and (f) $(120, 240)_{\sigma}$.

be extended to other low lattice symmetry 2D materials. Furthermore, the discovery of abundant GBs greatly enriches our limited knowledge of the atomic structure of 2D materials and can provide an ideal platform to explore structure-related GB properties and applications.

3. Experimental Section

Synthesis and Transfer of ReS_2: Monolayer ReS_2 film was synthesized using a CVD growth approach similar to the previously reported work.[41] Briefly, freshly cleaved mica substrates were placed at the center of a ceramic boat containing ReO_3 (10 mg; Sigma-Aldrich, 99.9%). Some crushed molecular sieves were spread evenly over the ReO_3, and then it was placed into a quartz tube. Sulfur powder (60 mg, Sigma-Aldrich, 99.5%) was placed at varying distances of 6–10 cm from the furnace center so as to maintain it at 200 °C for growth temperatures of 600–800 °C. The furnace was heated to the growth temperature at the rate of 25 °C min^{-1} under 50 sccm Ar used as a carrier gas, and then kept at the growth temperature for 10 min. After growth, the furnace was naturally cooled to room temperature. The as-grown ReS_2 samples were transferred by a polymethyl methacrylate-assisted process in hot (70 °C) deionized water onto a Cu grid for STEM analysis or onto SiO_2/Si substrates for Raman spectral analysis and electrical properties tests.

Optical and Raman Characterization of ReS_2: The as-grown ReS_2 samples were characterized by optical microscopy (Olympus BX51), and Raman spectroscopy, a single spectrum was collected for each acquisition with acquisition time of 10 s with an 1800 grooves mm^{-1} grating. Spatial Raman mapping was performed using a WITec RSA 300+ Raman spectrometer, wavelength of the excitation laser was 532 nm and the laser power was maintained at 2 mW. The laser spot size was ≈1 μm and focused through an objective lens 100× (numerical aperture 0.90). Angle-resolved polarized Raman experiments were performed via the approach similar to the previous work,[45] a polarizer was placed in the incident laser path to obtain the *x*-direction polarized light, and the polarized Raman spectra were obtained by rotating the laser polarization direction using a half-wave plate. AFM (Bruker Dimension ICON) was used to determine the thickness of the films.

STEM Characterization: All STEM images were taken at 80 kV on an aberration corrected FEI Titan Cubed G2. Before taking a photo, the samples were irradiated by electron beam for 20 min to reduce carbon deposition. SAED pattern and high-resolution bright images were taken in plain view with screen electricity 0.045 nA. The gather half angle was 25.1 mrad with a collect half angle of 260 mrad.

Device Fabrication and Electrical Characterization: Electrical contacts (5 nm Cr/50 nm Au, e-beam evaporated) were patterned by electron beam lithography on the ReS_2 sample. Electrical transport properties were measured in ambient air using Agilent B2912A sourcemeter unit.

Density Functional Calculations: All the calculations were performed within the framework of DFT implemented in the Vienna ab initio simulation package. Generalized gradient approximation parameterized by the Perdew–Burke–Ernzerh of functional was chosen to describe the electronic exchange and correlation items. The interaction between valence electrons and ion cores was included in the projected augmented wave method with the cutoff energy set at 258.7 eV. In order to modify the contributions of the van der Waals interaction and spin polarization, the Grimme DFT-D2 method and spin polarization were both considered. Integration over the Brillouin zone was performed using the Monkhorst–Pack method. Electronic iterations were required to be converged if the energy difference of the system between two iterations was less than 0.1 meV per atom. All the structures were optimized within the recommended conjugate gradient algorithm until the maximum force component on each atom reached the limit less than 0.01 eV $Å^{-1}$.

Supporting Information

Supporting Information is available from the Wiley Online Library or from the author.

Acknowledgements

X.B.L. and X.W. contributed equally to this work. This work was supported by the National Natural Science Foundation of China (51502167 and 51972204), the Natural Science Basic Research Plan in Shaanxi Province (No. 2018JQ5192), the Science and Technology Program of Shaanxi Province (No. 2017KJXX-16), the Fundamental Research Funds for the Central Universities in Shaanxi Normal University (GK201802003 and 2017TS048), and the Fundamental Research Funds for the Central Universities in Northwestern Polytechnical University (3102016QD071). The authors acknowledge the support from the Institute for Basic Science (IBS-R019-D1) of Korea. The authors also greatly acknowledge the usage of IBS-CMCM high performance computing system, Cimulator.

Conflict of Interest

The authors declare no conflict of interest.

Keywords

anisotropy, grain boundary, rhenium disulfide, subdomain, superlattices

Received: August 5, 2019
Revised: August 29, 2019
Published online: September 30, 2019

[1] A. Azizi, X. Zou, P. Ercius, Z. Zhang, A. L. Elías, N. Perea-López, G. Stone, M. Terrones, B. I. Yakobson, N. Alem, *Nat. Commun.* **2014**, *5*, 4867.
[2] R. G. Deng, X. L. Su, Z. Zheng, W. Liu, Y. G. Yan, Q. J. Zhang, V. P. Dravid, C. Uher, M. G. Kanatzidis, X. F. Tang, *Sci. Adv.* **2018**, *4*, eaar5606.
[3] P. Y. Huang, C. S. Ruiz-Vargas, A. M. van der Zande, W. S. Whitney, M. P. Levendorf, J. W. Kevek, S. Garg, J. S. Alden, C. J. Hustedt, Y. Zhu, J. Park, P. L. McEuen, D. A. Muller, *Nature* **2011**, *469*, 389.
[4] T. H. Ly, D. J. Perello, J. Zhao, Q. M. Deng, H. Kim, G. H. Han, S. H. Chae, H. Y. Jeong, Y. H. Lee, *Nat. Commun.* **2016**, *7*, 10426.
[5] L. Lin, B. Deng, J. Y. Sun, H. L. Peng, Z. F. Liu, *Chem. Rev.* **2018**, *118*, 9281.
[6] K.-C. Kim, J. Lee, B. K. Kim, W. Y. Choi, H. J. Chang, S. O. Won, B. Kwon, S. K. Kim, D.-B. Hyun, H. J. Kim, H. C. Koo, J.-H. Choi, D.-I. Kim, J.-S. Kim, S.-H. Baek, *Nat. Commun.* **2016**, *7*, 12449.
[7] Z. H. Zhang, X. L. Zou, V. H. Crespi, B. I. Yakobson, *ACS Nano* **2013**, *7*, 10475.
[8] Y. L. Huang, Y. F. Chen, W. J. Zhang, S. Y. Quek, C.-H. Chen, L.-J. Li, W.-T. Hsu, W.-H. Chang, Y. J. Zheng, W. Chen, A. T. S. Wee, *Nat. Commun.* **2015**, *6*, 6298.
[9] W. Bao, N. J. Borys, C. Ko, J. Suh, W. Fan, A. Thron, Y. J. Zhang, A. Buyanin, J. Zhang, S. Cabrini, P. D. Ashby, A. Weber-Bargioni, S. Tongay, S. Aloni, D. F. Ogletree, J. Wu, M. B. Salmeron, P. J. Schuck, *Nat. Commun.* **2015**, *6*, 7993.
[10] V. K. Sangwan, D. Jariwala, I. S. Kim, K.-S. Chen, T. J. Marks, L. J. Lauhon, M. C. Hersam, *Nat. Nanotechnol.* **2015**, *10*, 403.
[11] X. G. Fan, S. Wagner, P. Schädlich, F. Speck, S. Kataria, T. Haraldsson, T. Seyller, M. C. Lemme, F. Niklaus, *Sci. Adv.* **2018**, *4*, eaar5170.
[12] A. L. Gibb, N. Alem, J.-H. Chen, K. J. Erickson, J. Ciston, A. Gautam, M. Linck, A. Zettl, *J. Am. Chem. Soc.* **2013**, *135*, 6758.
[13] J. Cheng, T. Jiang, Q. Ji, Y. Zhang, Z. Li, Y. Shan, Y. Zhang, X. Gong, W. Liu, S. Wu, *Adv. Mater.* **2015**, *27*, 4069.
[14] H.-P. Komsa, A. V. Krasheninnikov, *Adv. Electron. Mater.* **2017**, *3*, 2199.
[15] A. M. van der Zande, P. Y. Huang, D. A. Chenet, T. C. Berkelbach, Y. You, G.-H. Lee, T. F. Heinz, D. R. Reichman, D. A. Muller, J. C. Hone, *Nat. Mater.* **2013**, *12*, 554.
[16] S. Najmaei, Z. Liu, W. Zhou, X. Zou, G. Shi, S. Lei, B. I. Yakobson, J.-C. Idrobo, P. M. Ajayan, J. Lou, *Nat. Mater.* **2013**, *12*, 754.
[17] S. Tongay, H. Sahin, C. Ko, A. Luce, W. Fan, K. Liu, J. Zhou, Y.-S. Huang, C.-H. Ho, J. Y. Yan, D. F. Ogletree, S. Aloni, J. Ji, S. S. Li, J. B. Li, F. M. Peeters, J. Q. Wu, *Nat. Commun.* **2014**, *5*, 3252.
[18] H. Cai, B. Chen, G. Wang, E. Soignard, A. Khosravi, M. Manca, X. Marie, S. L. Y. Chang, B. Urbaszek, S. Tongay, *Adv. Mater.* **2017**, *29*, 1605551.
[19] S. Cho, S. Kim, J. H. Kim, J. Zhao, J. Seok, D. H. Keum, J. Baik, D.-H. Choe, K. J. Chang, K. Suenaga, S. W. Kim, Y. H. Lee, H. Yang, *Science* **2015**, *349*, 625.
[20] Y. F. Sun, Y. X. Wang, D. Sun, B. R. Carvalho, C. G. Read, C.-h. Lee, Z. Lin, K. Fujisawa, J. A. Robinson, V. H. Crespi, M. Terrones, R. E. Schaak, *Angew. Chem., Int. Ed.* **2016**, *55*, 2830.
[21] S. L. Jiang, M. Hong, W. Wei, L. Y. Zhao, N. Zhang, Z. P. Zhang, P. F. Yang, N. Gao, X. B. Zhou, C. Y. Xie, J. P. Shi, Y. H. Huan, L. M. Tong, J. J. Zhao, Q. Zhang, Q. Fu, Y. F. Zhang, *Commun. Chem.* **2018**, *1*, 17.
[22] S. L. Jiang, Z. P. Zhang, N. Zhang, Y. H. Huan, Y. Gong, M. X. Sun, J. P. Shi, C. Y. Xie, P. F. Yang, Q. Y. Fang, H. Li, L. M. Tong, D. Xie, L. Gu, P. R. Liu, Y. F. Zhang, *Nano Res.* **2018**, *11*, 1787.
[23] M. Rahman, K. Davey, S.-Z. Qiao, *Adv. Funct. Mater.* **2017**, *27*, 1606129.
[24] Y.-C. Lin, H.-P. Komsa, C.-H. Yeh, T. Björkman, Z.-Y. Liang, C.-H. Ho, Y.-S. Huang, P.-W. Chiu, A. V. Krasheninnikov, K. Suenaga, *ACS Nano* **2015**, *9*, 11249.
[25] D. A. Chenet, O. B. Aslan, P. Y. Huang, C. Fan, A. M. van der Zande, T. F. Heinz, J. C. Hone, *Nano Lett.* **2015**, *15*, 5667.
[26] E. Z. Zhang, Y. B. Jin, X. Yuan, W. Y. Wang, C. Zhang, L. Tang, S. S. Liu, P. Zhou, W. D. Hu, F. X. Xiu, *Adv. Funct. Mater.* **2015**, *25*, 4076.
[27] F. Liu, S. Zheng, X. He, A. Chaturvedi, J. He, W. L. Chow, T. R. Mion, X. Wang, J. Zhou, Q. Fu, H. J. Fan, B. K. Tay, L. Song, R.-H. He, C. Kloc, P. M. Ajayan, Z. Liu, *Adv. Funct. Mater.* **2016**, *26*, 1169.
[28] E. F. Liu, Y. J. Fu, Y. J. Wang, Y. Q. Feng, H. M. Liu, X. G. Wan, W. Zhou, B. G. Wang, L. B. Shao, C.-H. Ho, Y.-S. Huang, Z. Y. Cao, L. G. Wang, A. D. Li, J. W. Zeng, F. Q. Song, X. R. Wang, Y. Shi, H. T. Yuan, H. Y. Hwang, Y. Cui, F. Miao, D. Y. Xing, *Nat. Commun.* **2015**, *6*, 6991.
[29] N. N. Mao, S. S. Zhang, J. X. Wu, H. H. Tian, J. X. Wu, H. Xu, H. L. Peng, L. M. Tong, J. Zhang, *Nano Res.* **2018**, *11*, 3154.
[30] M. Kertesz, R. Hoffmann, *J. Am. Chem. Soc.* **1984**, *106*, 3453.
[31] Y. Q. Fang, J. Pan, J. Q. He, R. C. Luo, D. Wang, X. L. Che, K. J. Bu, W. Zhao, P. Liu, G. Mu, H. Zhang, T. Q. Lin, F. Q. Huang, *Angew. Chem., Int. Ed.* **2018**, *57*, 1232.
[32] K. D. Wu, B. Chen, S. J. Yang, G. Wang, W. Kong, H. Cai, T. Aoki, E. Soignard, X. Marie, A. Yano, A. Suslu, B. Urbaszek, S. Tongay, *Nano Lett.* **2016**, *16*, 5888.
[33] M. Hong, X. B. Zhou, N. Gao, S. L. Jiang, C. Y. Xie, L. Y. Zhao, Y. Gao, Z. P. Zhang, P. F. Yang, Y. P. Shi, Q. Zhang, Z. F. Liu, J. J. Zhao, Y. F. Zhang, *ACS Nano* **2018**, *12*, 10095.
[34] M. Hafeez, L. Gan, H. Li, Y. Ma, T. Zhai, *Adv. Mater.* **2016**, *28*, 8296.
[35] A. T. Hoang, S. M. Shinde, A. K. Katiyar, K. P. Dhakal, X. Chen, H. Kim, S. W. Lee, Z. Lee, J.-H. Ahn, *Nanoscale* **2018**, *10*, 21978.
[36] L. Hart, S. Dale, S. Hoye, J. L. Webb, D. Wolverson, *Nano Lett.* **2016**, *16*, 1381.
[37] F. F. Cui, C. Wang, X. B. Li, G. Wang, K. Q. Liu, Z. Yang, Q. L. Feng, X. Liang, Z. Y. Zhang, S. Z. Liu, Z. B. Lei, Z. H. Liu, H. Xu, J. Zhang, *Adv. Mater.* **2016**, *28*, 5019.

[38] V. I. Artyukhov, Y. Liu, B. I. Yakobson, *Proc. Natl. Acad. Sci. USA* **2012**, *109*, 15136.
[39] X. L. Zou, Y. Y. Liu, B. I. Yakobson, *Nano Lett.* **2013**, *13*, 253.
[40] X. X. He, F. C. Liu, P. Hu, W. Fu, X. L. Wang, Q. S. Zeng, W. Zhao, Z. Liu, *Small* **2015**, *11*, 5423.
[41] X. B. Li, F. F. Cui, Q. L. Feng, G. Wang, X. S. Xu, J. X. Wu, N. N. Mao, X. Liang, Z. Y. Zhang, J. Zhang, H. Xu, *Nanoscale* **2016**, *8*, 18956.
[42] K. Keyshar, Y. J. Gong, G. L. Ye, G. Brunetto, W. Zhou, D. P. Cole, K. Hackenberg, Y. He, L. Machado, M. Kabbani, A. H. C. Hart, B. Li, D. S. Galvao, A. George, R. Vajtai, C. S. Tiwary, P. M. Ajayan, *Adv. Mater.* **2015**, *27*, 4640.
[43] M. Hafeez, L. Gan, H. Q. Li, Y. Ma, T. Y. Zhai, *Adv. Funct. Mater.* **2016**, *26*, 4551.
[44] Q. K. Yu, L. A. Jauregui, W. Wu, R. Colby, J. F. Tian, Z. H. Su, H. L. Cao, Z. H. Liu, D. Pandey, D. G. Wei, T. F. Chung, P. Peng, N. P. Guisinger, E. A. Stach, J. Bao, S.-S. Pei, Y. P. Chen, *Nat. Mater.* **2011**, *10*, 443.
[45] J. X. Wu, N. N. Mao, L. M. Xie, H. Xu, J. Zhang, *Angew. Chem., Int. Ed.* **2015**, *54*, 2366.